

The Reverberation Chamber's Unstirred Field: A Validation of the Image Theory Interpretation

Ryan J. Pirkl¹, John M. Ladbury², and Kate A. Remley³

National Institute of Standards and Technology
Electromagnetics Division
Boulder, Colorado 80305, USA

¹ryan.pirkl@nist.gov

²john.ladbury@nist.gov

³kate.remley@nist.gov

Abstract—Synthetic aperture measurements of a reverberation chamber's unstirred wireless channel are used to compare the observed power, time-of-arrival, and angle-of-arrival of unstirred multipath components to that predicted by ray/image theory for a rectangular cavity. An examination of the ray paths corresponding to erroneously predicted unstirred multipath components revealed that these ray paths intersect the reverberation chamber's mode-stirring paddles, absorber blocks, and various other objects in the chamber. This inspired a simple image-blocking model for the reverberation chamber's unstirred wireless channel, whereby contributions from ray paths intersecting the chamber's mode-stirring paddles and absorbers are neglected. This model elucidates the unstirred wireless channel's geometry-based multipath structure, justifies established best practices for reverberation chamber measurements, and enables the development of more effective techniques for mitigating the reverberation chamber's unstirred field components.

Index Terms—image theory, ray theory, reverberation chamber, unstirred field

I. INTRODUCTION

THE accuracy of conventional radiated emissions and susceptibility measurements in reverberation chambers is degraded by the presence of multipath components that are unperturbed by mode-stirring techniques [1]. For mechanical stirring methodologies, these *unstirred* field contributions are most commonly associated with the line-of-sight propagation path between two antennas [2]–[4]. This direct path is often the dominant multipath component in the reverberation chamber's unstirred wireless channel, but it is unlikely to be the only unstirred propagation path [3], [5], [6]. Depending on the geometry of the measurement configuration, ground and wall bounces present additional propagation paths that may be unperturbed by mechanical stirring.

Here, we use wideband synthetic aperture measurements to discern the underlying multipath structure of the reverberation chamber's unstirred wireless channel. A comparison of the time- and angle-of-arrival of the observed multipath components to that predicted by ray/image theory for a rectangular cavity reveals a simple geometric interpretation of the chamber's unstirred multipath components in which ray paths that intersect the stirrers (and other objects in the

reverberation chamber) are neglected. Section II begins with a description of the synthetic aperture measurements conducted within the reverberation chamber. Then, in Section III, we use these synthetic aperture measurements to calculate the reverberation chamber's unstirred power delay-angle spectrum, which describes the time- and angle-of-arrival of the chamber's unstirred multipath components. In Section IV, we compare the reverberation chamber's unstirred power delay-angle spectrum to the power, time-of-arrival, and angle-of-arrival of multipath components as predicted by ray/image theory for the corresponding rectangular cavity problem. Large errors in the predicted multipath structure of the unstirred wireless channel are traced to ray paths that intersect objects in the environment. This leads to the image-blocking model for the unstirred wireless channel presented and evaluated in Section V. Implications of this image-blocking model and conclusions are discussed in Section VI.

II. SYNTHETIC APERTURE MEASUREMENTS

Synthetic aperture measurements are characterized by a non-stationary antenna that is scanned through space so as to record the spatial variations of a signal within a specified observation region. The resulting space-dependent data set may then be used with conventional array processing techniques, including angle-of-arrival analyses [7], [8]. The setup for the reverberation chamber synthetic aperture measurements is depicted in Fig. 1. The measurements were conducted within a 3.60 m by 4.27 m by 2.90 m reverberation chamber featuring a pair of rotating paddles. The paddle rotating about a vertical axis swept a cylindrical volume 2.46 m high and 1.00 m in diameter; the paddle rotating about a horizontal axis swept a cylindrical volume 3.3 m long and 1.00 m in diameter. The angular resolution of the controller for each stirrer was 0.1°.

A vertically polarized biconical antenna served as the “scan” antenna for the synthetic aperture measurements. The scan antenna was mounted at a height of 70 cm atop an 18 cm high 2-D positioner capable of scanning a 0.5 m by 0.5 m planar region. This positioned the biconical antenna's radiating element 0.98 m from the reverberation chamber's floor. The “source” antenna for the synthetic aperture measurements was a stationary and vertically polarized discone antenna posi-

U. S. government work not subject to U. S. copyright.

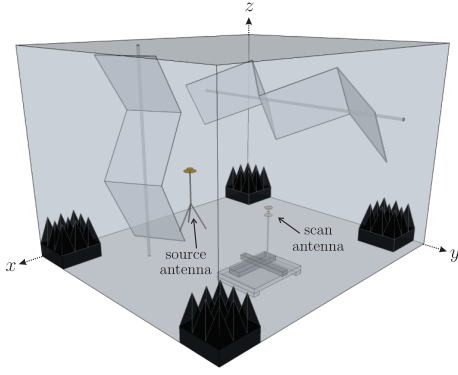


Fig. 1. Diagram of the synthetic aperture measurements conducted within a reverberation chamber.

tioned 2.1 m away from the scan antenna at an identical height of 0.98 m. The source and scan antennas were connected to ports #1 and #2, respectively, of a vector network analyzer (VNA), which was calibrated at the antenna ports. The scan antenna was stepped along a 2 cm uniform rectangular grid within the 2-D positioner's 0.5 m by 0.5 m scan region. At each scan antenna position, both paddles were stepped in 12° increments through a full 360° , resulting in thirty unique paddle angles. The spatial resolution of the 2-D positioner was $6.35 \mu\text{m}$. To reduce multiple scattering between the scan antenna and the reverberation chamber, four 0.6 m by 0.6 m by 0.6 m three-by-three pyramidal absorber blocks were placed near the chamber's corners.

At each observation point and paddle angle, complex S_{21} measurements were recorded from 1 to 6 GHz at 781 kHz intervals. The manufacturer-specified uncertainty in the magnitude and phase of an S_{21} measurement was 0.2 dB and 0.1° , respectively. We denote the S_{21} data as $S_{21}(f, \mathbf{r}, n)$ where f denotes the frequency, \mathbf{r} denotes the scan antenna's position, and $n = 1, \dots, 30$ denotes the thirty unique paddle angles. Reverberation chamber measurements of the source and scan antennas' free-space reflection coefficients, $\Gamma_1(f)$ and $\Gamma_2(f)$, respectively, were used to correct for the impedance mismatch of the antennas (see [9]). We define this mismatch-corrected S_{21} data as the reverberation chamber's wireless channel $h(f, \mathbf{r}, n)$:

$$h(f, \mathbf{r}, n) = \frac{S_{21}(f, \mathbf{r}, n)}{\sqrt{1 - |\Gamma_1(f)|^2} \sqrt{1 - |\Gamma_2(f)|^2}}. \quad (1)$$

III. UNSTIRRED POWER DELAY-ANGLE SPECTRUM

The reverberation chamber's *unstirred* wireless channel, denoted $\bar{h}(f, \mathbf{r})$, was determined by averaging the wireless channel over the thirty paddle angles:

$$\bar{h}(f, \mathbf{r}) = \langle h(f, \mathbf{r}, n) \rangle_n. \quad (2)$$

From this unstirred wireless channel, we may calculate the reverberation chamber's corresponding unstirred *power delay-angle spectrum*, denoted $P_{\bar{h}}(\tau, \phi)$, which provides a general

description of the time-of-arrival (i.e., delay) τ , azimuth angle-of-arrival ϕ , and power contributed by the reverberation chamber's unstirred multipath components. We first calculate the 2-D space- and frequency-dependent wireless channel's power delay-wavevector spectrum, $P_{\bar{h}}(\tau, \mathbf{k})$, which is given by the magnitude-squared of the channel's frequency and 2-D spatial Fourier transform [10]:

$$P_{\bar{h}}(\tau, \mathbf{k}) = \left| \iint \bar{h}(f, \mathbf{r}) e^{j2\pi\tau f} e^{j\mathbf{k}\cdot\mathbf{r}} df d\mathbf{r} \right|^2, \quad (3)$$

where \mathbf{k} denotes wavevector. Expressing \mathbf{k} in cylindrical coordinates as $\mathbf{k} = (k, \beta)$, whereby the power delay-wavevector spectrum is denoted as $P_{\bar{h}}(\tau, k, \beta)$, and assuming that only homogeneous plane waves contribute to the observed channel, we define the corresponding power delay-angle spectrum $P_{\bar{h}}(\tau, \phi)$ as

$$P_{\bar{h}}(\tau, \phi) = \int_0^\infty P_{\bar{h}}(\tau, k, \phi + \pi) k dk, \quad (4)$$

where we have mapped the spectral components' direction-of-propagation β to angle-of-arrival ϕ .

Figure 2 presents a portion of the unstirred channel's power delay-angle spectrum corresponding to $\tau < 22$ ns. The power delay-angle spectrum was normalized to a maximum value of 0 dB. By propagating the uncertainty in $\bar{h}(f, \mathbf{r})$ through (3)-(4), the maximum uncertainty in the power delay-angle spectrum presented in Fig. 2 (and later in Figs. 4 and 7) was determined to be 1.4 dB for $P_{\bar{h}}(\tau, \phi) > -50$ dB, where -50 dB is approximately the mean of the variance-based noise floor. The uncertainty in $\bar{h}(f, \mathbf{r})$ was determined from the variance of $h(f, \mathbf{r}, n)$ as calculated with respect to the thirty unique paddle angles. The corresponding minimum signal-to-noise ratio for $P_{\bar{h}}(\tau, \phi) > -50$ dB was 5.5 dB. Each "pulse" in the spectrum indicates the azimuth angle, delay, and relative power of one or more multipath components incident on the scan region. It should be noted that due to the finite spatial and temporal resolution of the measurements, as well as the absence of elevation angle-of-arrival information, it is impossible to determine if a given pulse corresponds to a single multipath component or a tightly grouped cluster of multipath components with similar time- and angle-of-arrival characteristics.

As noted in the figure, the first pair of pulses at approximately $\tau = 7$ ns and 10 ns for $\phi = 250^\circ$ correspond to the line-of-sight (LOS) path and its corresponding ground-bounce path, respectively. The subsequent pair of labeled pulses at approximately $\tau = 11$ ns and 13 ns for $\phi = 260^\circ$ correspond to a wall-bounce path and its corresponding ground-bounce path, respectively. Figure 3 illustrates the ray paths corresponding to these four early-time multipath components. As we will show in the proceeding sections, much of the unstirred wireless channel's multipath structure may be explained through a continuation of this ray/image theory representation of the reverberation chamber problem.

IV. IMAGE THEORY REPRESENTATION OF A RECTANGULAR CAVITY

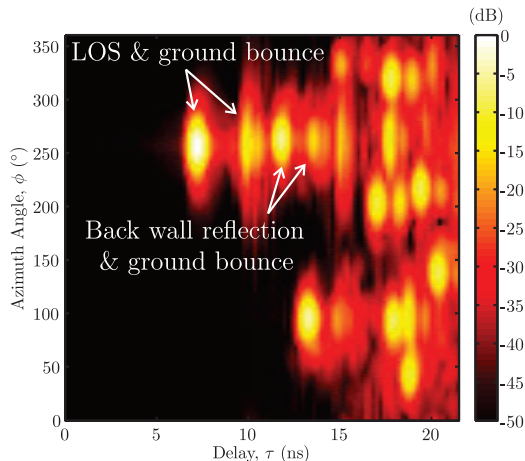


Fig. 2. The reverberation chamber's early-time unstirred power delay-angle spectrum calculated from measurements of the unstirred wireless channel.

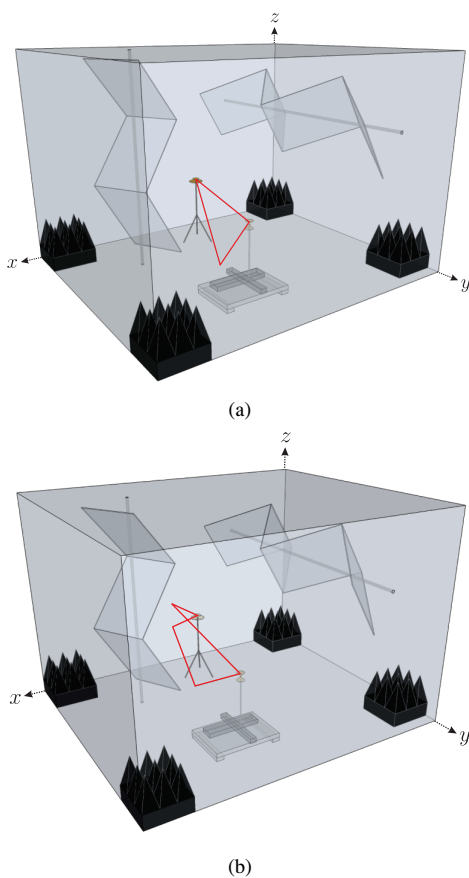


Fig. 3. Early time propagation paths: (a) LOS with corresponding ground-bounce and (b) reflection off of the back wall with corresponding ground-bounce.

Image theory and the closely related ray theory have previously been used to study the electromagnetic field within rectangular cavities so as to infer the characteristics of a corresponding reverberation chamber [5], [11]–[13]. However, application of these techniques to the more geometrically complex mechanically stirred reverberation chamber problem has generally been avoided due to the high computational cost. A notable exception is [5], which used ray theory to analyze the field within a vibrating (i.e., moving wall) reverberation chamber. Here, we will compare the observed multipath structure of the reverberation chamber's unstirred wireless channel to that predicted by ray/image theory for the corresponding rectangular cavity problem. Our implementation is based on image theory, which offers a simple mathematical description of the source image lattice (see Appendix A). However, as with Fig. 3, our discussion will generally favor ray theory, because it is more easily visualized and more physically intuitive.

Figure 4 compares the early-time unstirred wireless channel's power delay-angle spectrum to that predicted by image theory. Each circle identifies the delay and azimuth angle of waves incident on the observation region due to the i th source image located at \mathbf{r}_i . For the i th image, the corresponding multipath component's delay τ_i is

$$\tau_i = \|\mathbf{R}_i\|/v_p, \quad (5)$$

where v_p is the free-space propagation velocity of electromagnetic waves and \mathbf{R}_i is a vector pointing from the observation (i.e., scan) region's center, denoted \mathbf{r}_{obs} , to the i th source image's location:

$$\mathbf{R}_i = \mathbf{r}_i - \mathbf{r}_{\text{obs}}. \quad (6)$$

The azimuth angle-of-arrival, ϕ_i , of the i th source image's corresponding multipath component was determined from the x - and y -components of \mathbf{R}_i .

The shade of each circle indicates the power contributed by a given source image assuming a $1/\|\mathbf{R}_i\|^2$ path loss dependence. In addition, both antennas were assumed to have a dipole-like $\sin^2(\theta)$ power gain pattern, where θ denotes the zenith angle with respect to the z -axis. Thus, the power P_i contributed by the i th source image was

$$P_i = \frac{\sin^4(\theta_i)}{\|\mathbf{R}_i\|^2}, \quad (7)$$

where θ_i is the zenith angle-of-arrival of the i th image as determined from \mathbf{R}_i . Note that (7) implicitly accounts for the gain pattern of both of the co-polarized antennas. To facilitate comparisons between the observed and predicted multipath components' powers, image theory's predicted powers P_i were further scaled such that the power contributed by the original radiating source (i.e., the line-of-sight ray path) was 0 dB.

We observe good agreement between the time- and angle-of-arrival of the measured unstirred multipath components and that predicted by image theory. In most cases, wherever there is a circle denoting the delay and azimuth angle of a source

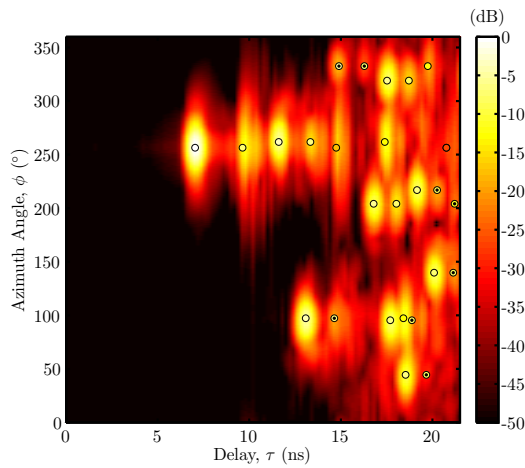


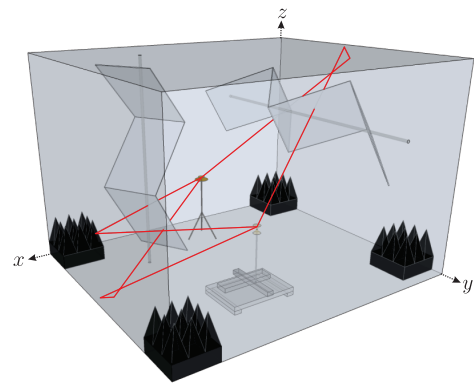
Fig. 4. Comparison of the unstirred power delay-angle spectrum with the power, time-of-arrival, and azimuth angle-of-arrival of unstirred multipath components as predicted by image theory for a rectangular cavity. The concentric dots identify images whose predicted power differs from the observed power by more than 10 dB.

image’s contribution, there is also a “pulse” in the power delay-angle spectrum. However, the agreement in terms of power levels is inconsistent. Although many of the source images’ power levels are close to the observed multipath components’ power levels, there are numerous instances where the predicted and observed power levels differ considerably. Using concentric dots, we have identified all of the source images in Fig. 4 whose predicted power differs from the observed power by more than 10 dB. Bicubic interpolation was used to interpolate the power delay-angle spectrum $P_{\bar{h}}(\tau, \phi)$ to each source image’s corresponding τ_i and ϕ_i . Importantly, we note that all eight of the “large” errors identified in Fig. 4 correspond to cases where image theory *overestimated* the power in the corresponding unstirred multipath component.

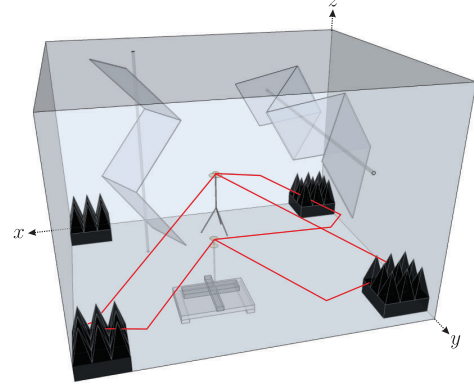
Figure 5 examines the ray paths corresponding to these eight erroneous source images. Note that all of the ray paths intersect and, presumably, are attenuated by an object in the environment. Figure 5(a) shows the ray paths that intersect the reverberation chamber’s mechanical paddles; Fig. 5(b), the absorber blocks; and Fig. 5(c), the 2-D positioner. We note that the shorter of the two ray paths in Fig. 5(c) does not actually intersect the 2-D positioner, but it does pass within about 2 cm of the positioner whereby the positioner is well within the ray path’s first Fresnel zone for 1-6 GHz.

V. AN IMAGE-BLOCKING MODEL FOR THE UNSTIRRED WIRELESS CHANNEL

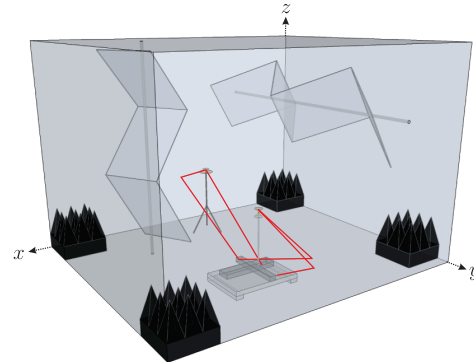
Figures 4-5 indicate that certain source images’ contributions to the unstirred wireless channel are attenuated due to interactions with various scatterers in the reverberation chamber. Taking this attenuation to the extreme, we consider a simple geometry-based image-blocking model for the reverberation chamber’s unstirred wireless channel that neglects contributions from images whose corresponding rays are obstructed by



(a) paths intersecting the mechanical stirrers



(b) paths intersecting the absorbers



(c) paths intersecting the 2-D positioner

Fig. 5. Early time propagation paths corresponding to the eight source images identified in Fig. 4 that overestimated the observed multipath components by more than 10 dB.

objects in the environment. For our image theory implementation, it is important to recognize that we are actually working with an infinite lattice of radiating sources *and* an infinite lattice of environment scatterers [12, Appendix G]. That is, to accurately employ this image-blocking model, we must determine if the path between the observation region’s center, \mathbf{r}_{obs} , and the i th source image’s location, \mathbf{r}_i is obstructed by not only the environment’s real scatterers (e.g., stirrers, absorbers, etc.) but also images of these scatterers.

To ease the computational burden in determining these ray-

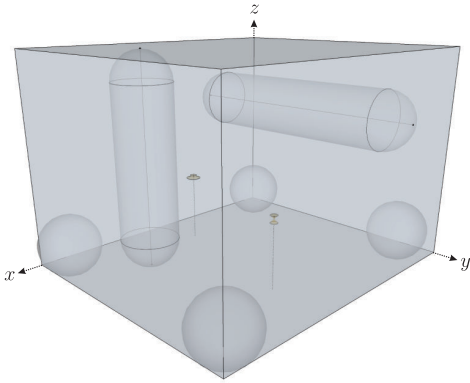


Fig. 6. Diagram of the simplified problem geometry used with the image-blocking model of the unstirred wireless channel.

object intersections, we use the simplified problem geometry shown in Fig. 6. We model the stirrers as 0.8 m diameter cylinders with hemispherical “caps.” This diameter is smaller than the 1.0 m diameter of the cylindrical volume swept by the stirrers, but it better accounts for the fact that ray paths intersecting a stirrer’s swept volume near the axis of rotation are far more likely to be obstructed than ray paths intersecting the swept volume near the periphery. The length of each cylinder was determined such that the top/bottom of the cylinders’ hemispherical caps touched the wall/floor/ceiling of the reverberation chamber. The four absorbers were modeled as minimum bounding spheres centered about the absorbers. (Note that these object representations are equivalent to a line-segment/point convolved with a sphere, whereby we may determine the occurrence of a ray-object intersection by comparing the sphere’s radius to the minimum distance between a ray path and an object’s line-segment/point.) Again favoring simplicity, we neglect the blocking effects of the 2-D positioner and other fixed objects (e.g., door handles, cables, antenna mounts, etc.) in the environment. Although, Fig. 4 indicates that these stationary scatterers affect the unstirred wireless channel, their irregularities and small dimensions make them considerably more difficult to model. Further reductions in computational cost were attained by restricting our analysis to multipath delays of less than 100 ns. This allowed us to truncate the nominally infinite source and scatterer image lattice to those source and scatterer images located approximately 30 m from the observation region.

Figure 7 compares the unstirred wireless channel’s power delay-angle spectrum to the power, time-of-arrival, and angle-of-arrival of multipath components as predicted by the image-blocking model. Overall, the structural agreement between the image-blocking model’s predicted power and the power delay-angle spectrum is seen to be quite good. There are a few cases where the image-blocking model suggests the occurrence of a strong multipath component, while the power delay-angle spectrum indicates no observed multipath component. These erroneous images are largely attributed to the inherent simplicity of the image-blocking model, wherein source images

are either neglected or left unaltered. Extending the simple geometric premise of this image-blocking model, one could easily construct a more nuanced model for the reverberation chamber’s unstirred wireless channel that partially attenuates source images depending on the geometry of the ray-object intersection and/or the material composition of the intersected object. It is expected that such higher complexity models will yield a more accurate prediction of the reverberation chamber’s unstirred wireless channel. Finally, as a crude quantitative evaluation of the image-blocking model’s accuracy, we determine the percentage of images with “large” errors (analogous to the percent of “dotted” images in Fig. 4). Restricting our analysis to $\tau < 100$ ns and defining an error as an image whose predicted power differs by more than 10 dB from the observed power, we observe a $51 \pm 7\%$ error rate for basic image theory as compared to a $22 \pm 4\%$ error rate for the image-blocking model. The uncertainties in these error percentages were determined from the uncertainty in the power delay-angle spectrum.

VI. CONCLUSIONS

Our simple geometry-based model for the reverberation chamber’s unstirred wireless channel provides justification for many established best practices for suppressing the reverberation chamber’s unstirred electromagnetic field and elucidates some of the fundamental limitations of these mitigation techniques. For example, orienting a pair of directional antennas away from each other has been shown to be an effective first step in reducing the unstirred power in reverberation chamber measurements [4], [14]. From our image-blocking model of the reverberation chamber’s unstirred wireless channel, we see that these directional antennas will heavily attenuate the LOS of path, as may be expected, but may *amplify* any unstirred ray paths whose angle-of-arrival and angle-of-departure correspond with both antennas’ main beams. Thus, the effectiveness of using directional antennas strongly depends on how these antennas and the corresponding “source” antenna images are oriented with respect to one another. As suggested in [15], the effectiveness of directional antennas may be improved by pointing their main beams toward the stirrers. From our image-blocking model, we see that this will effectively shunt power from the unobstructed ray paths to those blocked by the stirrers.

Our image-blocking model also suggests that the cross-sectional area swept by a stirrer is more important than the stirrer’s swept volume. The larger this cross-sectional area, the more ray paths that will be blocked (i.e., stirred) by the stirrers. In this light, reverberation chambers using multiple large wall-mounted planar stirrers (e.g., see [3], [16]) may be the most effective designs for mitigating the unstirred field contributions, because they will minimize the number of unobstructed ray paths. Finally, the image-blocking model enables the development of the first comprehensive reverberation chamber model that merges the reverberation chamber’s well-established stochastic stirred field models with the geometry-based deterministic structure of the chamber’s unstirred fields.

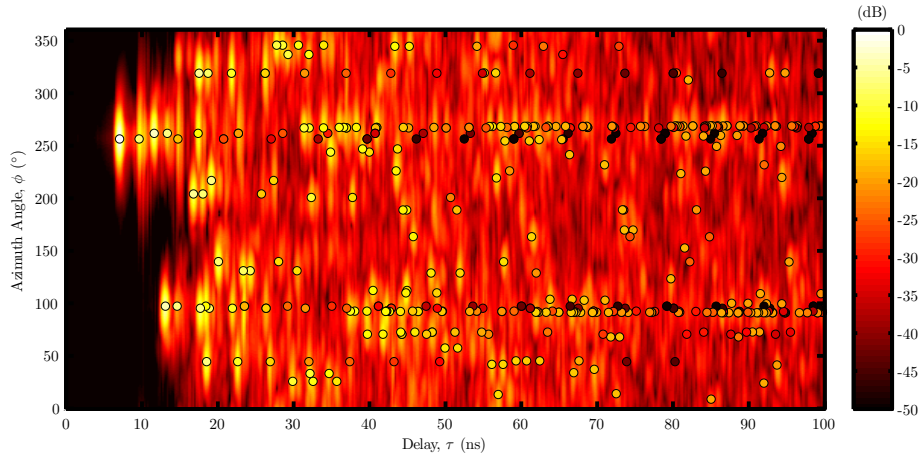


Fig. 7. The observed unstirred power delay-angle spectrum overlaid by dots indicating the power, time-of-arrival, and azimuth angle-of-arrival of unstirred multipath components as predicted by the image-blocking model.

APPENDIX A SOURCE IMAGE LATTICE

Assume a rectangular cavity aligned with the Cartesian coordinate system. The cavity volume spans the region defined by $0 < x < a$, $0 < y < b$, and $0 < z < c$ with bounding conducting walls at $x = 0, a$, $y = 0, b$, and $z = 0, c$. Further assume some infinitesimal radiating source at $\mathbf{r}_0 = (x_0, y_0, z_0)$ that is within the cavity volume. To determine the set of positions $\{\mathbf{r}_i\}$ of all of the sources in image theory's source lattice, we first define the positions $\mathbf{r}_0^{(p)}$ of eight sources defining the lattice's unit cell:

$$\mathbf{r}_0^{(p)} = (\pm x_0, \pm y_0, \pm z_0) \quad (8)$$

where $p = \{0, 1, \dots, 7\}$ identifies one of the eight unique combinations of $(\pm x_0, \pm y_0, \pm z_0)$ with the assumption that $\mathbf{r}_0^{(0)} = (x_0, y_0, z_0)$. The position \mathbf{r}_i of the i th source in the lattice is then given by

$$\mathbf{r}_i = \mathbf{r}_{\ell, m, n, p} = \mathbf{r}_0^{(p)} + 2a\ell\hat{\mathbf{x}} + 2bm\hat{\mathbf{y}} + 2cn\hat{\mathbf{z}}, \quad (9)$$

where $\hat{\mathbf{x}}$, $\hat{\mathbf{y}}$, and $\hat{\mathbf{z}}$ are the Cartesian coordinate system's three orthonormal vectors, $i = \{0, 1, 2, \dots, \infty\}$ is a single index that uniquely identifies each quadruple index (ℓ, m, n, p) , and $\ell, m, n = \{-\infty, \dots, -1, 0, 1, \dots, \infty\}$. For notational convenience, we have assumed that $i = 0$ corresponds to $(\ell, m, n, p) = (0, 0, 0, 0)$ whereby $\mathbf{r}_i|_{i=0}$ corresponds to the original source's location at \mathbf{r}_0 .

REFERENCES

- [1] V. M. Primiani, F. Moglie, and V. Paoletta, "Numerical and experimental investigation of unstirred frequencies in reverberation chambers," in *2009 IEEE International Symposium on Electromagnetic Compatibility*, Austin, TX, 17-21 August 2009, pp. 177–181.
- [2] P. Corona, G. Ferrara, and M. Migliaccio, "Reverberating chamber electromagnetic field in presence of an unstirred component," *IEEE Transactions on Electromagnetic Compatibility*, vol. 42, no. 2, pp. 111–115, May 2000.
- [3] K. Harima, "Determination of EMI antenna factor using reverberation chamber," in *2005 International Symposium on Electromagnetic Compatibility*, Chicago, IL, 12 August 2005, pp. 93–96.
- [4] C. L. Holloway, D. A. Hill, J. M. Ladbury, P. F. Wilson, G. Koepke, and J. Coder, "On the use of reverberation chambers to simulate a Rician radio environment for the testing of wireless devices," *IEEE Antennas and Propagation*, vol. 11, no. 11, pp. 3167–3177, November 2006.
- [5] N. K. Kouveliotis, P. T. Trakadas, and C. N. Capsalis, "Theoretical investigation of the field conditions in a vibrating reverberation chamber with an unstirred component," *IEEE Transactions on Electromagnetic Compatibility*, vol. 45, no. 1, pp. 77–81, February 2003.
- [6] V. M. Primiani and F. Moglie, "Numerical simulations of LOS and NLOS conditions for an antenna inside a reverberation chamber," *Journal of Electromagnetic Waves and Applications*, vol. 24, no. 17-18, pp. 2319–2331, 2010.
- [7] J. Fuhl, J.-P. Rossi, and E. Bonek, "High-resolution 3-D direction-of-arrival determination for urban mobile radio," *IEEE Transactions on Antennas and Propagation*, vol. 45, no. 4, pp. 672–682, April 1997.
- [8] J. Laurila, K. Kalliola, M. Toeltsch, K. Hugl, P. Vainikainen, and E. Bonek, "Wide-band 3-D characterization of mobile radio channels in urban environment," *IEEE Transactions on Antennas and Propagation*, vol. 50, no. 2, pp. 233–243, February 2002.
- [9] C. L. Holloway, D. A. Hill, M. Sandroni, J. M. Ladbury, J. S. Coder, G. Koepke, A. C. Marvin, and Y. He, "Use of reverberation chambers to determine the shielding effectiveness of physically small, electrical large enclosures and cavities," *IEEE Transactions on Electromagnetic Compatibility*, vol. 50, no. 4, pp. 770–782, November 2008.
- [10] G. D. Durgin, *Space-Time Wireless Channels*. Upper Saddle River, NJ: Prentice Hall Inc., 2003.
- [11] D.-H. Kwon, R. Burkholder, and P. Pathak, "Ray analysis of electromagnetic field build-up and quality factor of electrically large shielded enclosures," *IEEE Transactions on Electromagnetic Compatibility*, vol. 40, no. 1, pp. 19–26, February 1998.
- [12] D. A. Hill, *Electromagnetic Fields in Cavities: Deterministic and Statistical Theories*. Hoboken, NJ: John Wiley & Sons, Inc., 2009.
- [13] E. Amador, C. Lemoine, P. Besnier, and A. Laisné, "Reverberation chamber modeling based on image theory: investigation in the pulse regime," *IEEE Transactions on Electromagnetic Compatibility*, vol. 52, no. 4, pp. 778–789, November 2010.
- [14] J.-H. Choi, S.-O. Park, T.-S. Yang, and J.-H. Byun, "Generation of Rayleigh/Rician fading channels with variable RMS delay by changing boundary conditions of the reverberation chamber," *IEEE Antennas and Wireless Propagation Letters*, vol. 9, pp. 510–513, 2010.
- [15] O. Lundén and M. Bäckström, "How to avoid unstirred high frequency components in mode stirred reverberation chambers," in *IEEE International Symposium on Electromagnetic Compatibility*, Honolulu, HI, 9-13 July 2007, pp. 1–4.
- [16] P. Corona, G. Ferrara, and M. Migliaccio, "Reverberating chambers as a source of stochastic electromagnetic fields," *IEEE Transactions on Electromagnetic Compatibility*, vol. 38, no. 3, pp. 348–356, August 1996.